

# The Mechanical Behavior and Microstructure of a Multilayer Nanostructured Ni-Co Alloy Fabricated by Electrodeposition

Xiaoxue Zhang, Xixun Shen\*, Jiawen Chen

Shanghai Key Laboratory of Materials Protection and Advanced Materials in Electric Power, Shanghai Engineering Research Center of Energy-Saving in Heat Exchange Systems, Shanghai University of Electric Power, Shanghai 200090, PR China

\*E-mail: [shenxixun@shiep.edu.cn](mailto:shenxixun@shiep.edu.cn)

Received: 14 March 2021 / Accepted: 3 May 2021 / Published: 31 May 2021

---

A bulk multilayer nanostructured Ni-Co alloy with nano-grains (NG) layer with a thickness of 2.7 $\mu$ m and ultrafine grains (UFG) layer with a thickness of 0.9 $\mu$ m alternately grown is fabricated by an electrodeposition process. The analysis from X-ray diffractometer and transmission electron microscope reveal that the well-defined alternative layers consists of NG with a mean size of 23 nm with a random growth and UFG with a mean size of 90 nm along a (200) preferential growth. Tensile tests show that the multilayer nanostructured Ni-Co alloy exhibits an enhanced ductility with an elongation to failure of 14.2% and higher ultimate tensile strength of 1851MPa compared with the monolithic UFG and NG counterparts. The enhanced ductility for the multilayer nanostructured Ni-Co alloy is attributed to the improvement of work hardening ability brought by the action of the special microstructure involving the periodical distribution of UFG layer, the existence of interface and the alternation of crystal orientation between the layers in the dislocation activities and the effective adjustment to the local stress concentration brought by the periodic existence of the UFG layer in this layer structure. The higher strength sourced from the extra reinforcement provided by the hinder of interface to dislocation movement.

---

**Keywords:** Nanostructured Ni-Co alloy; Multilayer; Electrodeposition; Ductility; Strength

## 1. INTRODUCTION

Nanocrystalline (NC) metals with excellent mechanical strength and hardness have great application value in engineering [1-3]. However, this new class of material usually exhibit high strength but poor ductility, which becomes an obstacle to their widespread application. Therefore, how to improve the plasticity of NC metals has been one of the research hotspots in the field of material science in the past few decades. Many studies on experiments and simulations have implied that the low ductility of NC metals is attributed to its inherent low strain hardening ability that due to insufficient dislocation

activity in such a small nanoscale. The challenge posed by the inherent low ductility of NC metals has prompted researchers to increase the ductility by tailoring an uneven microstructure with a multimodal or bimodal grain size distribution in recent years. For example, Long et al. fabricated an ultrafine-grained (UFG) Ti–6Al–4V alloy with a bimodal microstructure composed of the equiaxed UFG with the grain size about 800 nm, the lamellar-structured coarse grains (CG) with the grain size of 20–70 $\mu$ m and recrystallized CG with the grain size of 2–5 $\mu$ m by means of the spark plasma sintering of the mixture of ball milled and unmilled powders. The bimodal alloy shows a high ultimate compressive strength of 2306 MPa and a large plastic strain to failure of 24% simultaneously [4]. Wang et al. prepared a mixed microstructured pure Cu with a grain size distribution between 25nm and 228nm by a low-temperature friction stirring process, in which the proportion of NG was about 45.3%. The nano/ultrafine grain structured pure Cu exhibited an enhanced ultimate tensile strength of 550 MPa, which was approximately three times than that of annealed Cu, and high tensile elongation of 25% [5]. By employing the process, other materials i.e. aluminum, magnesium and steels for structural applications have also been prepared [6-9]. Wang et al. created a bimodal grain size distribution nanostructured (NS) Cu of the micrometer-sized grains embedded inside a NG and UFG matrix by severe plastic deformed (SPD) and thermomechanical treatment. The matrix grains give high strength and the micron-sized grains provide the necessary strain hardening capacity for stable tensile deformation., which leads to a high tensile ductility~65% elongation to failure [10]. The above studies show that constructing heterogeneous microstructures with bimodal or multimodal distribution of grain size is an effective way to improve the plasticity of high-strength NC metals. From the above studies, it can be seen that the current methods for determining non-uniform microstructures are in principle based on a combination of severe plastic deformation and heat treatment. Although this process can construct heterogeneous microstructures composed of different grain sizes, it cannot accurately determine the proportion and distribution of different grain sizes. Obviously, from the perspective of practical engineering applications, it is necessary to be able to tailor the grain size proportion and distribution in a controlled manner when designing heterogeneous microstructures in order to flexibly determine the performance of the material.

Multilayer(ML)with a typical design feature of alternating stacking is a new class of material architecture that has prevailed in recent years for being engineered to improve the mechanical properties (such as hardness, strength and corrosion resistance) of the reinforced film and coating materials for mechanical application. In traditional ML architectures, immiscible metallic and/or ceramic species are usually selected for layering such that the geometric confinement imposed by layer interfaces is augmented by lattice misfit between constituents, leading to increases in interfacial barrier strength. Obviously, if alternate stacking of different grains can be used instead of alternate stacking of heterogeneous materials in such a layered structure design, the distribution and proportion of grains of different sizes in NS materials can be flexibly controlled by introducing structure parameters such as layer thickness and alternating periods. At present, physical vapour deposition(PVD) such as magnetron sputtering[11], vapor deposition[12], ion plating[13] have been employed to produce ML materials. These methods are suitable for preparing heterostructured ML materials, but it is difficult to control the inter-layer grain size. Compared to these physical deposition methods, electrodeposition (ED) is an attractive method due that it not only can adjust the grain size of material in a wide range by simple adjusting electroplating parameters, but also is suitable for manufacturing various materials [14-17].

Recently, Kurmanaeva et al. prepared ML Ni-Fe materials with a 5- $\mu\text{m}$ -layer thickness by pulsed ED technique. A modulated grain size distribution was maintained by the imposed pulses with average grain size of 16 and 500 nm in NG and CG sub-layers. However, this ML Ni-Fe sample does not exhibit optimized mechanical properties, and the plasticity obtained is even lower than that of the monolithic NG sample. The relatively unsatisfactory plasticity was found to be caused by the combination of face centered cubic (fcc) and body centered cubic (bcc) phases in the sample microstructures [18]. Subsequently, Matthew Daly et al. prepared a single-phase layered NS Ni-Co alloy with a layer thickness ratio of 1: 1 by pulse ED. Compared to uniform NG and CG samples, the ML Ni-Co alloy exhibits only compromised mechanical properties of  $\sim 1112\text{MPa}$  ultimate tensile strength and 6.9% elongation [19]. Such mechanical properties are actually similar to the recently reported uniform structure Ni-Co alloys. Recently, we designed a novel alternating deposition mode by periodically changing the current density during ED to achieve flexible regulation of the grain size and its distribution inside the material. By such an alternating deposition mode, two layered structure materials with clear grain size distribution were successfully prepared, namely a ML NS Cu consisting of 67nm NG and 200nm UFG with a layer thickness ratio of 10: 1 and a ML NS Ni composed of 20nm NG and 500nm UFG with a layer thickness ratio of 2: 1. Compared to homogeneous structural materials, the two layered NS materials we designed show superior mechanical properties. The ML NS Cu with a layer thickness ratio of UFG to NG is 1: 10 not only maintains a very high strength similar to that of its homogeneous NG counterpart but also exhibit a strong plastic deformation ability with a large elongation to failure close to that of UFG Cu. The designed ML NS Ni with the layer thickness ratio of UFG to NG is 1: 2 exhibits a large elongation to failure twice higher than that of the homogeneous NG Ni under maintaining moderate strength. Based on our current research and comparison, the mechanical properties of these ML NS Ni-based alloys prepared by the above-mentioned pulse ED have not been significantly optimized may be related to the mismatch between the grain size and the layer thickness ratio of the layers. For example, for the ML NS Ni-Co prepared by Matthew Daly et al. using pulse ED, the thickness of the single-layer NG layer and CG layer is about 10  $\mu\text{m}$  [19]. Such a large layer thickness makes the layers lose the ability to coordinate with each other during the deformation process, which may result in no significant improvement in plasticity. At the same time, the ultra-thick micron-scale grain layer as a large grain layer also leads to an excessive reduction in the strength, which obviously loses the advantage of the high strength of the NS materials. In addition, it is worth emphasizing that pulse ED still has certain limitations in regulating grain sizes. Therefore, based on the above analysis, in this article we use a direct current ED process to prepare a bulk ML NS Ni-Co alloy composed of NG layers and UFG layers instead of CG layers by changing the current density. Meanwhile, it is considered that the thickness of the sub-layer is too thick, which may lead to a weakened coordination ability between layers. Here, we obtain a Ni-Co alloy with a layer thickness ratio of about 3:1 by controlling the deposition time of each sublayer. The microstructures are studied by transmission electron microscopy (TEM) and X-ray diffractometer (XRD), and the mechanical properties are studied based on uniaxial tensile tests and the results are also compared with their counterparts of homogeneous structure.

## 2. EXPERIMENTAL

A bulk ML Ni-Co alloy sheet with a total thickness of about 600  $\mu\text{m}$  that composed of alternating NG layer and UFG layer according to a layer thickness ratio of 3: 1 was deposited on the stainless steel cathode sheet by periodically controlling two kinds of the current density from 15 to 3  $\text{Adm}^{-2}$  during ED at pH 4.7 and a temperature of 60  $^{\circ}\text{C}$ . We chose a sulfate bath containing nickel sulfate, nickel chloride, cobalt sulfate, boric acid and a small amount of additives. Two monolithic samples with the homogeneous structure were also fabricated at the corresponding current density of 3  $\text{Adm}^{-2}$  and 15  $\text{Adm}^{-2}$  for comparison. Then these as-deposited sheets were mechanically stripped from the stainless steel cathode and cut into corresponding specimens for characterization and mechanical tests. The scanning electron microscope (SEM, JSM-5600) was used to characterize the cross-sectional morphology of ML NS Ni-Co specimen. Energy dispersive spectroscopy (EDS) was also used for an identification of chemical composition of two sub-layers using line and point scanning. Microstructure and selected area diffraction (SAD) patterns of the cross-section of ML NS Ni-Co specimens and two monolithic specimens were investigated by the transmission electron microscope (TEM, a JEM-2100F). The thin specimen with the thickness of about 100 nm for TEM observation was cut by Tescan GAIA FIB-SEM with a Ga ion source at an accelerated voltage of 30 kV. X-ray diffractometer (XRD, Bruker D8) with a Cu  $K\alpha$  radiation (0.154178 nm) operating at 40 kV and 40 mA over the  $2\theta$  range 30–90 $^{\circ}$  was used to analyse the crystallographic structure of two sublayers of the ML NS Ni-Co specimen. The tensile tests were conducted on a tensile testing machine (UTM5105SYXL) at a strain rate of  $4.17 \times 10^{-2} \text{s}^{-1}$  at room temperature (RT). For tensile test, the dog-bone shaped tensile specimens with a gauge length of 8.0 mm and the cross-section of 2.0 mm  $\times$  0.5 mm are machined by using the wire electrical discharge machining and then were polished to a mirror-like finish surface. Then the work hardening rate (WHR) [ $\Theta = (d\sigma_{\text{true}}/d\delta_{\text{true}})/\sigma_{\text{true}}$ ] was also calculated in order to evaluate the work hardening effect corresponding to different microstructures. The fracture morphology and the deformed surface morphology of the ML NS Ni-Co specimens and two counterparts with the homogeneous structure were also observed by SEM.

## 3. RESULTS AND DISCUSSION

Figure 1(a) shows the cross-sectional SEM image of the as-deposited ML NS Ni-Co alloy after chemical etching. It can be clearly seen that the Ni-Co alloy exhibit a well-defined layered structure in which a deep gray layer of about 2.7  $\mu\text{m}$  and a light gray sunken one of about 0.9  $\mu\text{m}$  is alternately stacked. Based on the thickness of these two alternating layers combined with the currently applied electroplating process parameters, it can be roughly inferred that the deep gray layer should correspond to the plating layer formed at the current density of 15  $\text{Adm}^{-2}$  and the light gray layer should belong to that formed at 3  $\text{Adm}^{-2}$ . It has been suggested that applying a high current density during ED may refine the grain size of the coating. According to such an influence law, it can be further concluded that the deep gray layer of 2.7  $\mu\text{m}$  attained at 15  $\text{Adm}^{-2}$  belongs to the small grain sized layer while the deep gray layer with a thickness of 0.9  $\mu\text{m}$  attained at 3  $\text{Adm}^{-2}$  belongs to large grain sized layer. Considering that different

polarization behaviors of Ni and Co under two kinds of different current densities may bring about the difference in the composition of the alternating layer, the EDS line scanning and the point analysis are also performed along the cross-section of ML NS Ni-Co alloy. Figure 1(b) shows the energy spectrum curve of a line scan from a white straight line region across several consecutive alternating layers in Figure 1(a). It can be seen from Figure 1(b) that the line scanning energy spectrum curves of two elements both show a wave-shaped spectrum peak that fluctuates periodically with respect to the alternating layer, which means that the content of element Co and Ni in the alternating layer is greatly affected by the applied current density. Moreover, the line scan spectrum peaks of two elements also exhibit an opposite fluctuation behavior with respect to the alternating layers. As shown in Figure 1(b), the peak count intensity of element Ni for the plating layer formed at high current density is evidently greater than that corresponding to the plating layer formed at low current density while the peak intensity of the element Co corresponding to the alternating layer shows an opposite changing trend. As we know that Ni and Co deposits are anomalous, most current densities led to Co-rich depositions and only high currents favored the deposition of Ni. Such an opposite fluctuation behavior also further illustrates that the content of the element Ni and Co in the alternating layer shows an opposite change with the applied current density. The point-spectrum analysis is also performed to quantify the content of Ni and Co in two alternating layers. Figure 1(c) shows the point energy spectrum curves for two alternating layers and the corresponding results are summarized in Table 1. From Table 1, it can be seen that the contents of Ni and Co in the plating layer formed at the high current density are 78.12% and 21.82%, respectively, while their contents in the plating layer formed at the low current density are 72.9% and 27.1%.

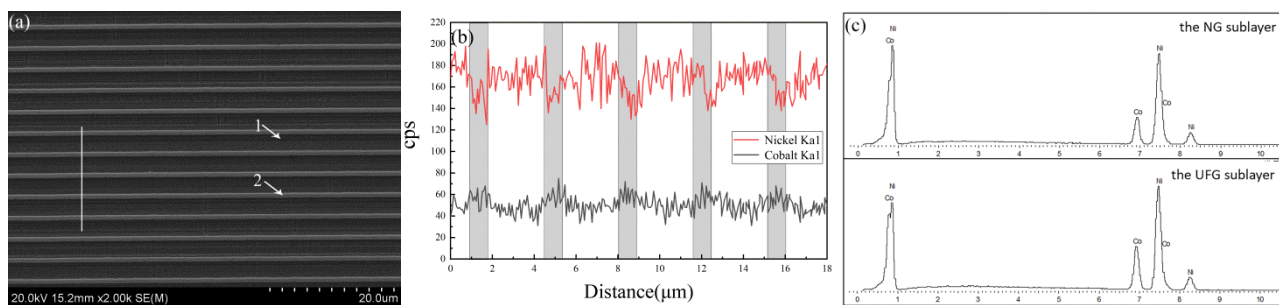


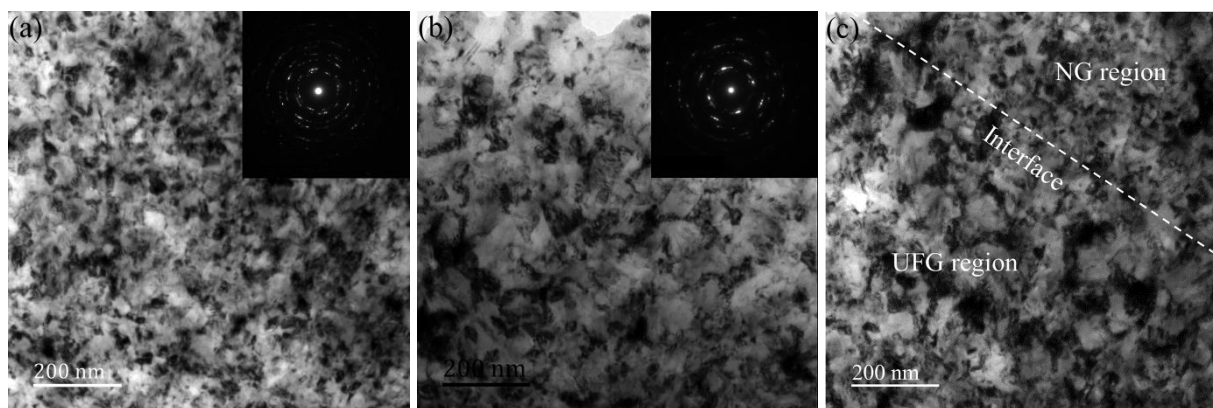
**Figure 1.** (a) The cross-section SEM image of the ML NS Ni-Co alloy obtained by alternating 3 and 15  $\text{Adm}^{-2}$ ; (b) SEM-EDS line scan across several layers as shown by the white line in (a); (c) SEM-EDS point scan on the NG sublayer obtained at 15  $\text{Adm}^{-2}$  and UFG sublayer obtained at 3  $\text{Adm}^{-2}$  as shown at points 1 and 2 in (a).

**Table 1.** The content (wt%) of Ni and Co element in the NG and UFG sublayer.

Region	Ni [wt%]	Co [wt%]
1(the NG sublayer)	78.18	21.82
2(the UFG sublayer)	72.90	27.10

Figure 2 shows the bright-field TEM images of the small sized grain layer, the large sized grain layer and the interface region of two alternating layers of the ML NS Ni-Co alloy. The SAD patterns

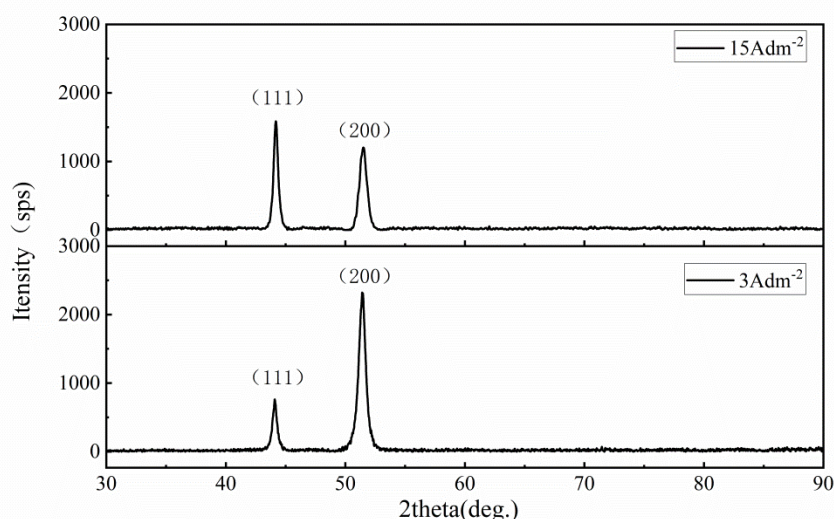
corresponding to two alternating layers are inserted. It can be seen from Figure 2(a) that the microstructure of small-sized grain layer is composed of nearly equiaxed grains and its grain size distribution ranging from 10nm to 40nm, a relatively small range. Based on the grain statistics of TEM images from several different regions, the average grain size for the small-sized grain layer is calculated to be about 23 nm. For the large-size grain layers as shown in Figure 2(b), the microstructure is also composed of equiaxed grains, but these equiaxed grains hold a wider size distribution of from 30 nm to 140 nm with a mean grain size of about 90nm, as shown in Figure 2(b). Such nanostructures with a wide grain size distribution seems to be easily formed at relatively low current density [22-24]. In the interface region of the alternating layers, as shown in Figure 2(c), the microstructure obviously transitions from a small equiaxed grain area with a narrow grain size distribution to a larger equiaxed grain area with the grain size distribution similar to that of the large grain sized layer, and the interface of the intermediate layer is shown by the white dashed line. Furthermore, the two sublayers are closely bonded together and no micro defects such as voids and gaps can be seen in the interlayer interface. Obviously, the high-quality sample is a prerequisite for carrying out research on the essential deformation behavior of the layered structure. In Figure 2(a) and (b), the inset SAD patterns show a transition from an evident continuous diffraction rings to a discontinuous diffraction rings, which is consistent with the change in grain size in ML Ni-Co alloy. The TEM analysis results further illuminate that such an intended ML Ni-Co with an alternating growth of two kinds of grains with different grain sizes in the typical nanoscale range was well achieved by ED technique.



**Figure 2.** Bright-field cross-sectional TEM micrographs corresponding to: (a) the NG layer obtained at  $15 \text{ Adm}^{-2}$ , (b) the UFG layer obtained at  $3 \text{ Adm}^{-2}$  and (c) the interface region of the ML NS Ni-Co alloy. The insets are the SAD patterns corresponding to the NG layer and the UFG layer.

Figure 3 shows the XRD patterns corresponding to the monolithic UFG and NG Ni-Co alloy to verify the possibility of different crystal structures in different single layers of ML NS Ni-Co alloy. It can be seen that both the NG layer and the UFG layer exhibit a single fcc phase, but they have significantly different preferential growth orientations. For the NG layer formed under high current density, the ratio of the diffraction intensity of  $I(111)/I(200)$  is 1.16, which shows a double preferential growth texture along the (111) and (200) crystal planes. While for the UFG layers formed at low current

density, a strong (200) preferred growth texture is clearly shown from the XRD pattern, where the  $I(111) / I(200)$  is initially estimated to be only 0.285. The refractive index (2.05) of isotropic polycrystalline samples is known, 0.285 is nearly an order of magnitude lower. Also recently reported the observation of electrodeposited Ni-Co are similar to the texture of such grain growth [25-26]. The above texture transition coincides with the contrast change of the diffraction rings of the two-size grain layers shown in Figure 2, where for the NG layer, the contrast intensity of the first diffraction ring corresponding to (111) is basically equivalent to that of the second diffraction ring (200), while the contrast intensity of (111) from the UFG layer is significantly lower than that of its second diffraction ring (200). From the above XRD analysis we can know that in addition to the periodic variation of the grain size, the crystal growth direction also exhibits a preferred (200) crystal growth corresponding to the UFG layer and a near random crystal growth corresponding to the NG layer along the layered periodic transition of the cross section of ML NS Ni-Co alloy.

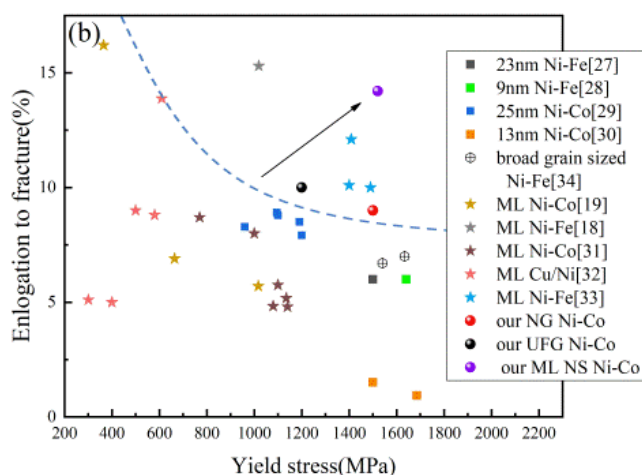
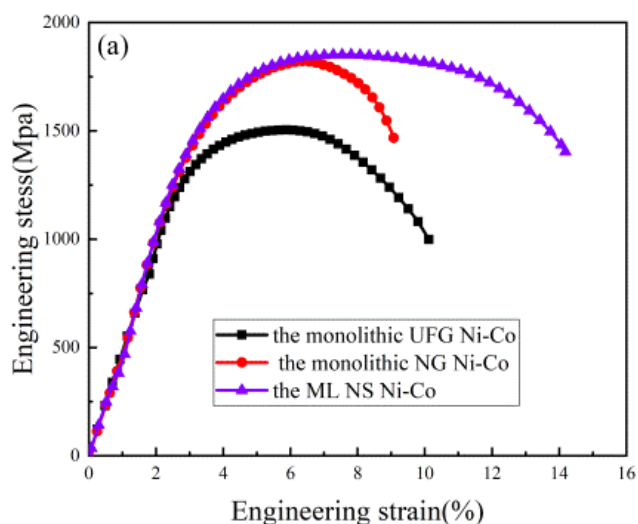


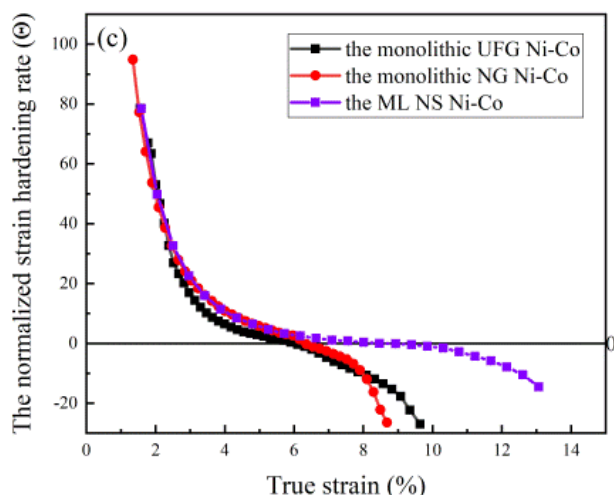
**Figure 3.** The XRD patterns of the monolithic UFG Ni-Co alloy obtained at  $15 \text{ Adm}^{-2}$  and NG Ni-Co alloy obtained at  $3 \text{ Adm}^{-2}$

Figure 4(a) presents tensile engineering stress–strain curves of the ML NS Ni-Co alloy, monolithic UFG and NG Ni-Co alloy at strain rate of  $4.17 \times 10^{-2} \text{ s}^{-1}$  and room temperature. All three specimens showed complete elastoplastic deformation behavior from the elastic stage to the plastic stage and to the final fracture in tension, which illustrates that the material prepared by the ED process has high quality. Although they exhibit similar plastic deformation behavior, the mechanical properties are obviously different in the stretching process. The ultrahigh tensile strength of UFG Ni-Co alloy is about 1504MPa and the elongation at break is about 10%. While the monolithic NG Ni-Co alloy has high ultrahigh tensile strength of about 1828MPa and a lower elongation to fracture of about 9%. The low ductility for the monolithic UFG and NG Ni-Co alloy is related to the plastic instability, that is, premature necking, as shown in Figure 4(a), these two samples exhibited a rapid necking behavior after a small uniform plastic deformation of less than 6%. While for the ML Ni-Co alloy, such necking behavior is

significantly suppressed and a large elongation to fracture of 14.2% and a uniform elongation of 8.4% are obtained. Previously reported heterogeneous NS materials have demonstrated a significantly improved plasticity at the expense of strength. However, it is exciting that the mechanical strength of the ML NS Ni-Co alloy constructed here does not decrease but keep close to 1851 MPa or even higher than monolithic NG Ni-Co alloy. Figure 4(b) summarizes the elongation to fracture and yield stress for NG and ML Ni-based alloys from literatures [18,19,27-34] and present study for comparison. The dotted line serves as a guide to distinguish both high strength and good ductility. It can be seen that the previous reported-NG and composite NS Ni-based alloys are located near or below the trend line, showing low strength or low ductility. In addition, the previous Ni-based alloys with a narrow grain size distribution [27-30], which are located near the dotted line or in the lower right corner, indicating that although the strength is acceptable, their ductility is poor. For previously reported Ni-based alloys with composite structures including wide grain size distribution or ML structures[18,19, 31-34], the intersection points of the elongation to fracture and yield strength are above or to the left of the dotted line, which indicates that the ductility can be greatly improved by constructing a composite nanostructure. By contrast, the intersection point of the ML NS Ni-Co alloy is away from the trend line, where our ML NS Ni-Co alloy exhibits a more prominent high tensile ductility at similar high strength level compared with these previous Ni-based alloys with whether homogeneous nanostructures or multilayer structures. The plastic instability of materials is related to the lack of effective strain hardening ability, Fig.4(c) shows the normalized WHR [ $\Theta = (d\sigma_{\text{true}}/d\delta_{\text{true}}) / \sigma_{\text{true}}$ ] of the ML, the monolithic UFG and NG Ni-Co alloy plotted as a function of true strain. It can be clearly seen that the normalized WHR of the NG and that of UFG Ni-Co quickly drop to zero only after a smaller uniform strain less than 6.2%. In comparison with the monolithic counterparts, the ML NS Ni-Co alloy has a longer-lasting strain hardening ability as shown in Figure 4(b), the positive normalized WHR is maintained to a larger uniform strain level of about 8.4%. The high strain hardening ability exhibited by the ML Ni-Co alloy in comparison with the monolithic counterparts with uniform structure can be attributed to the following several extra strengthening effects produced by such a special layered structure. The more durable strain hardening ability exhibited by ML NS Ni-Co alloys first comes from the contribution of large-sized UFG that are periodically incorporated into the NG matrix. These UFG with large geometries can facilitate the generation of dislocation and the appropriate dislocation accumulation [10,19,35]. Furthermore, it can be imagined that compared to the randomly distributed large-sized grains from previous reported inhomogeneous NS materials with the bimodal or broad grain size distribution, these regularly-arranged large-sized grain layers will provide a more uniform strain hardening behavior during the plastic deformation. Another strengthening factor contributing to the improvement of strain hardening ability is the contribution from the interface between the NG and UFG layer. This interface provides a source of dislocations and also hinders the transfer of dislocations between layers, thereby further improving the strain hardening ability[36]. And the change in the crystal preferred growth orientation between sublayers can lead to a discontinuous slip interface, which requires a higher resolution shear stress to transfer single dislocation across the interface. Additionally, the local stress concentration can be effectively suppressed by the coordinated deformation provided by the periodically incorporated UFG layer, which also further promote the plastic deformation ability. Such a layered structure can not only optimize the plastic deformation ability of the material, but also give the material higher strength. The higher strength exhibited by our ML NS Ni-Co alloy

compared to the monolithic NG components is attributed to the additional reinforcement provided by the interfaces that are periodically distributed inside the matrix. The existence of these interfaces will effectively hinder the movement of dislocations and provide additional strengthening for the matrix, which compensates for the decrease in the strength caused by the increase in the average grain size of the matrix sourced from the incorporation of UFG. As a result, a higher strength was obtained for the ML Ni-Co ally we designed compared to the monolithic NG components. But it should be also emphasized that in the previous studies on interface strengthening, the layer thickness in the designed ML structure materials was mostly limited to the nanometer level of tens of nanometers or even a few nanometers in order to obtain greater interface strengthening effects. Such a designed ML structure can obtain ultra-high strength and hardness, the nano-scale layer thickness greatly constrains dislocation activity and causes the ability to coordinate plastic deformation between layers. Here the ML structure composed of micron-sized thick NG layers and sub-micron-sized thick UFG layers we designed not only maintains a higher strength than the monolithic NG matrix, but also gives the material higher strain hardening ability to maintain greater plastic deformation.





**Figure 4.** (a) The engineering tensile stress-strain curves of the ML NS Ni-Co alloy obtained by alternating 3 and 15  $\text{Adm}^{-2}$ , the monolithic UFG and NG Ni-Co alloy obtained at 3 and 15  $\text{Adm}^{-2}$  respectively at a strain rate of  $4.17 \times 10^{-2} \text{s}^{-1}$  at room temperature. (b) Comparison of elongation to fracture vs. yield stress for NG and ML Ni-based alloys from literatures and present study. (c) The normalized work-hardening rate ( $\Theta = (d\sigma_{\text{true}}/d\delta_{\text{true}})/\sigma_{\text{true}}$ ) plotted as a function of true strain for the present three specimens.

This means that an appropriate layer thickness and layer thickness ratio are necessary when designing the ML structure to optimize the mechanical properties.

Figure 5 shows the surface morphology of the deformed region near the fracture front of the ML NS Ni-Co alloy, the monolithic UFG and NG Ni-Co alloy. It can be seen from Figure 5(a) that the monolithic UFG Ni-Co alloy exhibits an evident deformation trace with collapse and bulge surface feature near the fracture. Moreover, from the local magnification observation of the edge region near fracture shown in Figure 5(b) and that of the region with a certain distance from the fracture shown in Figure 5(c), it can be further known that such a shear deformation band with collapse and bulge feature is particularly serious near the edge region of the fracture and while in the region far from the fracture, relatively shallow deformation marks are presented.

This feature means that a larger non-uniform deformation happens near the fracture front, which corresponds to the early necking behavior of the monolithic UFG Ni-Co alloy exhibits during tension. Such local shear deformation bands concentrated near the edge of the fracture were also observed in previous reported UFG materials [21,37]. The surface area near the fracture of NG Ni-Co alloy is shown in Figure 5(d), a flat and smooth surface feature and only shallower fold-like shear deformation zone parallel to the crack direction appears near the fracture front. It can be identified by the local enlargement of the edge near the fracture as shown in Figure 5(e), which is consistent with the low ductility exhibited by the monolithic NG Ni-Co alloy. For the ML NS Ni-Co alloy, as shown in Figure 5(g), the dislocation slip-induced surface shear bands appear again.

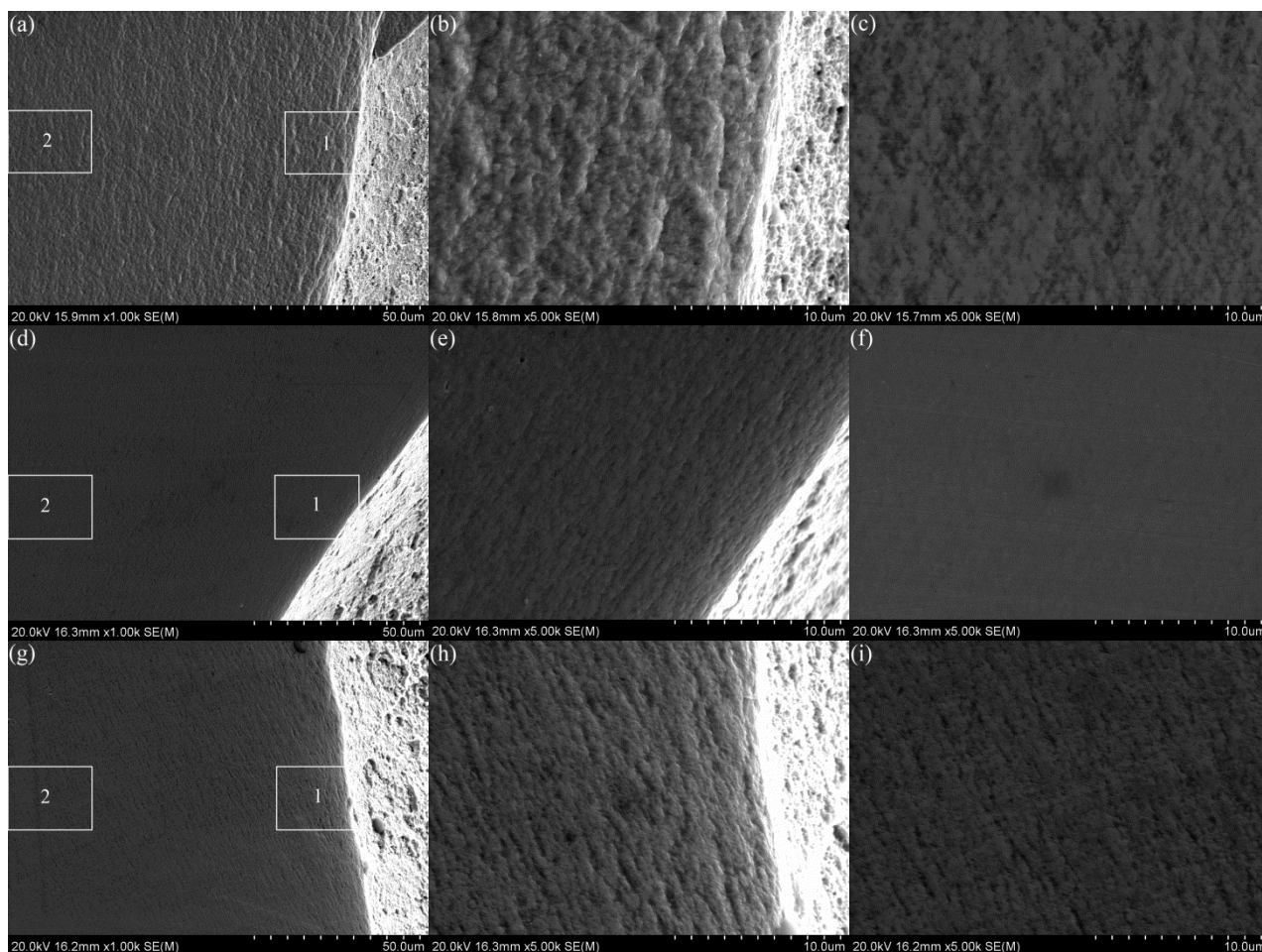


**Figure 5.** (a)The surface morphologies of deformed region near fracture front of the monolithic UFG Ni-Co alloy obtained at  $3 \text{ Adm}^{-2}$ , (b) and(c)The local magnification image of deformed region that the front of fracture and far from the fracture as marked by boxes; (d)The surface morphologies of monolithic NG Ni-Co alloy obtained at  $3 \text{ Adm}^{-2}$ , (e) and(f)The local magnification image of deformed region that the front of fracture and far from the fracture as marked by boxes; (g)The surface morphologies of deformed ML NS Ni-Co alloy obtained by alternating 3 and  $15 \text{ Adm}^{-2}$ . (h) and(i)The local magnification image of deformed region that the front of fracture and far from the fracture as marked by boxes.

However, in comparison with the monolithic UFG Ni-Co alloy, the ML Ni-Co alloy has a shear deformation zone with shallow collapse and uplift characteristics and furthermore, it can be seen from the magnified observation of Figure 5(h) and (i) that the shear deformation band for the ML NS Ni-Co alloy is relatively evenly distributed over the entire detected surface region. Such surface morphology feature furthermore implies that the ML NS Ni-Co alloy has a more uniform deformation capacity than the monolithic NG and UFG counterparts.

Figure 6 shows the fracture surface morphologies of the monolithic UFG Ni-Co alloy, the monolithic NG Ni-Co alloy and the ML NS Ni-Co alloy. It can be seen from Figure 6(a) that the monolithic UFG Ni-Co alloy shows an protuberance fracture surface with an inhomogeneous dimple structure consisting of an equiaxed dimple with an average size of about 500 nm and a distinct elongated deep dimple with the length size close to about 1200 nm distributed along zigzag ridge-like fracture

regions formed by crack propagation as marked by the white arrow. Such an protuberance fracture with an inhomogeneous dimple structure means that the monolithic UFG Ni-Co alloy undergoes a large non-uniform deformation during the fracture process, which is obviously consistent with the severe local shear deformation band concentrated near the fracture front that observed in the fracture surface. The monolithic NG Ni-Co alloy, as shown in Fig.6(b), exhibits a flat fracture surface with a shallow and small dimple structure, indicating a relatively small deformation experience, which is consistent with the relatively low tensile plasticity exhibited by the monolithic NG Ni-Co alloy during tension. Furthermore, the dimple structure also shows uneven distribution characteristics, as shown by the local magnification in Figure 6(b), where two types of dimple structures with significantly different sizes, i.e., one dimple structure with the size less than 200 nm and another with the size close to 500-600 nm were identified. Similar fracture feature with inhomogeneous dimple structure has also been observed in previously reported monolithic NG Ni [21]. For the ML NS Ni-Co alloy, an obvious layered fracture with two alternating fracture zones with different appearance feature corresponding to the layered structure can be seen from Figure 6(c). The fracture region corresponding to the narrow UFG layer, as indicated by the white arrow in Fig.(c), exhibits an erected fence-like narrow deformation band with the large dimples that have long edges and deep pits. Such fence-like deformation band indicates that the UFG layer undergoes a large deformation during tension. While the fracture region corresponding to the wider NG layer does not show a relatively flat fracture surface with an uneven dimple structure like that shown in the monolithic NG Ni-Co alloy, but exhibits a convex-concave fracture surface with more uniform and smaller dimple structure with the average dimple size less than 200 nm, as shown in the local magnification in Figure 6(c). Such an obvious change in the fracture feature of the NG layer illustrates that the incorporation of the UFG layer has a great influence on the fracture behavior of the NG matrix. It is well known that the dimple structure is formed by the expansion and coalescence of micro-voids induced by the stress concentration caused by the entanglement and intersection of a large number of transgranular dislocations or the interaction of transgranular dislocations with the second phase in the conventional CG metals. Recently, it has been suggested that in NG substrates, the generation and action mechanism of transgranular dislocations like that occurs in CG counterpart will be suppressed, and the grain boundary becomes the source of dislocation generation and at the same time the barrier to dislocation movement[38-39], which results in a larger stress concentration being preferentially formed at these defects especially at the triple grain boundary due to the lack of effective dislocation during deformation[40]. Under such a stress environment, the fracture of NG metal needs to be completed through several processes. First, the micropores generated at the grain boundaries extend along the intergranular path to a scale larger than the crystal grains, and then the micropores merge, which eventually leads to the shear fracture of the remaining ligaments. Additionally, because of the uneven deformation of NC metal, it is impossible to establish a uniform stress field near each crystal grain, which will lead to the difference in the distances of the expansion path of these micro-voids in NG matrix. This may be the reason for the flat fracture feature with a shallow inhomogeneous dimple structure larger than tens of times the grain size in the monolithic NC Ni-Co alloy matrix. Obviously, for the NG layer from the ML NS Ni-Co alloy, the local large stress field caused by the non-uniform deformation of NG can be effectively alleviated due to the alternate existence and cooperative deformation of the UFG layer. In such an environment, micro-voids will no longer preferentially

generated under the large stress field distributed in some local areas, but form in a balanced manner under a more evenly distributed small stress field. Meantime, the expansion process of these micro-voids changes with the change of the stress field environment. Driven by such a uniform small stress field, these micro-voids will relatively slowly expand and merge with through the coordination of short-range local slip of movable dislocations, which may result in the formation of a relatively uplifted fracture with a small dimple in the NG layer.

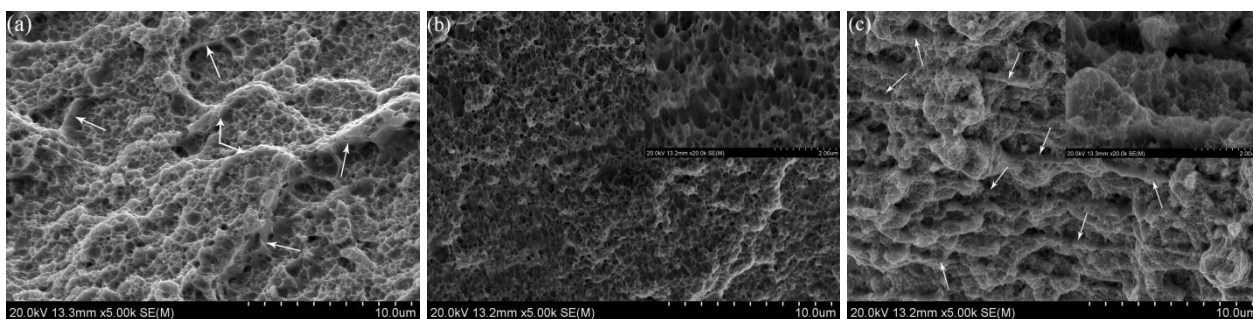


**Figure 6.** The fracture surface SEM images of specimens after tension: (a) the monolithic UFG Ni-Co alloy obtained at  $3 \text{ Adm}^{-2}$ , (b) the monolithic NG Ni-Co alloy obtained at  $15 \text{ Adm}^{-2}$  and (c) the ML NS Ni-Co alloy obtained by alternating  $3$  and  $15 \text{ Adm}^{-2}$ .

#### 4. CONCLUSIONS

A bulk multilayered Ni-Co alloy composed of the NG layer with a thickness of  $2.7 \mu\text{m}$  and the UFG layer with a thickness of  $0.9 \mu\text{m}$  alternately grow is successfully prepared by periodically controlling the current density during electrodeposition. This multilayered Ni-Co alloy has a higher tensile ductility without loss of high strength compared to the monolithic UFG and NG counterparts. The improvement of work hardening ability and the effective adjustment to the local stress concentration induced by the periodic existence of the UFG layer in NG matrix stabilizes the plastic deformation and then contribute to a larger tensile ductility. At the same time, the periodic incorporation of UFG layers also brings additional interface strengthening to the substrate, ensuring high tensile strength of the substrate. This work provides a novel strategy to optimize the mechanical property of NS materials.

#### ACKNOWLEDGEMENTS

This work was financially supported by National Natural Science Foundation of China (No. 21673135 and No. 21972090) and Science and Technology Commission of Shanghai Municipality (No. 17020500700, 18511110902 and 19DZ2271100).

#### References

1. L. Lu, Y. Shen, X. Chen, L. Qian and K. Lu, *Science*, 304(2004) 422.
2. Y. T. Zhu and X. Liao, *Nature Mater.*, 3 (6) (2004) 351.
3. T. Zhu, H. Gao, *Scr. Mater.*, 66(2012) 843.
4. Y. Long, T. Wang, H. Y. Zhang and X. L. Huang, *Mater. Sci. Eng. A*, 608 (2014) 82.
5. Y. P. Wang, R. D. Fu, X.Y. Zhou, G. B. Thompson, Z.Z. Yu and Y. J. Li, *Mater. Lett.*, 185(2016) 546.

6. F. Khodabakhshi, A. P. Gerlich, A. Simchi and A. H. Kokabi, *Mater. Sci. Eng. A*, 620(2015) 471.
7. A. Yazdipour, K. Dehghani, *Sci. Eng. A*, 527(2009) 192.
8. M. I. Costa, D. Verdera, M. T. Vieira and D. M. Rodrigues, *Appl. Surf. Sci.*, 296(2014)214.
9. V.V. Patel, W. Y.Li, A. Vairis and V. Badheka, *Crit. Rev. Solid State Mater. Sci.*, 44(2019) 378.
10. Y. Wang, M. Chen, F. Zhou and E. Ma, *Nature*, 419(2002) 912.
11. M. Petrantoni, C.Rossi, L. Salvagnac, V. Conedera, A. Esteve, C. Tenailleau and Y. J. Chabal, *J. Appl. Phys.*, 108(2010) 084323.
12. D.P. Zhou, H. Peng, L. Zhu, H.B. Guo and S.K. Gong, *Surf. Coat. Technol.*, 258(2014) 102.
13. A. J.Waldorf, J. A. Dobrowolski, B. T. Sullivan and L. M. Plante, *Appl. Opt.*, 32(1993) 5583.
14. I. Matsui, T. Kawakatsu, Y. Takigawa, T. Uesugi, and K. Higashi, *Mater. Lett.*, 116(2014) 71.
15. H. Mori, I. Matsui, Y. Takigawa, T. Uesugi and K. Higashi, *Mater. Lett.*, 175(2016) 86.
16. I. Matsui, H. Mori, T. Kawakatsu, Y. Takigawa, T. Uesugi and K. Higashi, *Mater. Sci. Eng. A*, 607( 2014) 505.
17. I. Matsui, Y. Takigawa, T. Uesugi, and K. Higashi, *Mater. Sci. Eng. A*, 578(2013) 318.
18. L. Kurmanaeva, H. Bahmanpour, T. Holland, J. Mccrea, J. H. Lee, J. Jian, and A. K. Mukherjee, *Philos.Mag.*, 94(2014) 3549.
19. M. Daly, J. L. Mccrea, B. A. Bouwhuis, C. V. Singh and G. D. Hibbard, *Mater. Sci. Eng. A*, 641(2015) 305.
20. B. Zheng, X.X. Shen, H.S. Jiao, Q.J. Xu, D.H. Cheng, *Adv. Eng. Mater.*, 20(2017)1700849.
21. X.X. Shen, M. Wu, D.M. Ji, Q.J. Xu and D.H. Cheng, *Mater. Sci. Eng. A*, 713( 2018) 43.
22. S. Pathak, M. Guinard, M. G. Vernooij, B. Cousin, Z. Wang, J. Michler and L. Philippe, *Surf. Coat. Techno.*, 205( 2011) 3651.
23. U. Sarac, M. C. Baykul and Y. Uguz, *J. Supercond. Novel Mag.*, 28( 2015)1041
24. X.X.Shen, J.S.Lian, Z.H. Jiang and Q. Jiang, *Adv. Eng. Mater.*, 10(2008) 539.
25. G. D. Hibbard, K. T. Aust and U. Erb, *Mater. Sci. Eng. A*, 433(2006) 195.
26. L.Y.Qin, J.S.Lian and Q.Jiang, *J. Alloys. Compd.*, 504(2010)s439
27. G. J. Fan, Y. D. Wang, L. F. Fu, H. Choo, P. K. Liaw, Y. Ren and N. D. Browning, *Appl. Phys. Lett.*, 88(2006) 5743.
28. H. Li and F. Ebrahimi, *Appl. Phys. Lett.*, 84(2004)4307.
29. C.D. Gu, J. S. Lian and Z.H. Jiang, *Adv. Eng. Mater.*, 8(2006) 252.
30. C.D. Gu, J. S. Lian, Q. Jiang and Z. H. Jiang, *Mater. Sci. Eng. A*, 59 ( 2007) 75.
31. M. Daly, S. Haldar, V. K. Rajendran, J. McCrea, G. D. Hibbard and C. V. Singh, *Mater. Sci. Eng. A*, 771( 2020)138581.
32. M. Tayyebi and B. Eghbali, *Mater. Sci. Eng. A*, 559( 2013) 759.
33. J. Fiebig, J. Jian, L. Kurmanaeva, J. McCrea, H. Wang, E. Lavernia and A. Mukherjee, *Mater. Sci. Eng. A*, 656( 2016) 174.
34. H. Li and F. Ebrahimi, *Acta Mater.*, 54( 2006) 2877.
35. E. Ma, *Scr. Mater.*, 49(2003) 663.
36. P. M. Anderson and C. Li, *Nanostruct. Mater.*, 5 (1995) 349.
37. S. J. Xie, P. K. Liaw and H. Choo, *J. Mater. Sci.*, 41(2006)6328.
38. X.X. Shen, C.C. Zhang, T. Zeng, D.H.Cheng and J.S.Lian, *Int. J. Mod. Phys. B*, 28(2014)1450124.
39. X.X. Shen, C.D. Gu, J.S. Lian, Q. Jiang, Z.H. Jiang and L.Y. Qin, *J. Appl. Phys.*, 108(2010)054319.
40. I. A. Ovid'ko and A. G. Sheinerman, *Appl. Phys. Lett.*, 90(2007) 171927.